Nano Research
2024, 17(4): 3189–3197

ISSN 1998-0124 CN 11-5974/O4
https://doi.org/10.1007/s12274-023-6163-3

Research Article

Design of advanced porous silver powder with high-sintering activity to improve silicon solar cells

Yongsheng Li[1,§], Ziwei Chen[1,§], Rui Zhou[1], Wenguang Zhao[1], Mu Li[2], Jun Chen[3], Zhongyuan Huang[1], Jian Liu[1], Yuhang Li[5], Maolin Yang[1], Minghan Yu[6], Dong Zhou[2] (✉), Yuan Lin[4] (✉), and Feng Pan[1] (✉)

[1] *School of Advanced Materials, Peking University, Shenzhen Graduate School, Shenzhen 518055, China*
[2] *Institute of Advanced Science Facilities, Shenzhen 518107, China*
[3] *Institute of Zhejiang University-Quzhou, Quzhou 324000, China*
[4] *Key Laboratory of Photochemistry, Institute of Chemistry, Chinese Academy of Sciences, Beijing 100190, China*
[5] *Institute of Materials Research (IMR), Tsinghua University, Tsinghua Shenzhen International Graduate School, Shenzhen 518055, China*
[6] *School of Materials Science and Engineering, Harbin Institute of Technology (Shenzhen), Shenzhen 518055, China*
[§] *Yongsheng Li and Ziwei Chen contributed equally to this work.*

Received: 9 July 2023 / **Revised:** 31 August 2023 / **Accepted:** 5 September 2023

ABSTRACT

Silver (Ag) paste is widely used in semiconductor metallization, especially in silicon solar cells. Ag powder is the material with the highest proportion in Ag paste. The morphology and structure of Ag powder are crucial which determine its characteristics, especially for the sintering activity. In this work, a simple method was developed to synthesize a type of microcrystalline spherical Ag particles (SP-A) with internal pores and the structural changes and sintering behavior were thoroughly studied by combining ultra-small-angle X-ray scattering (USAXS), small-angle X-ray scattering (SAXS), *in-situ* heating X-ray diffraction (XRD), focused ion beam (FIB), and thermal analysis measurement. Due to the unique internal pores, the grain size of SP-A is smaller, and the coefficient of thermal expansion (CTE) is higher than that of traditional solid Ag particles. As a result, the sintering activity of SP-A is excellent, which can form a denser sintered body and form silver nanoparticles at the Ag–Si interface to improve silver silicon contact. Polycrystalline silicon solar cell built with SP-A obtained a low series resistance (R_s) and a high photoelectric conversion efficiency (PCE) of 19.26%. These fill a gap in Ag particle structure research, which is significant for the development of high-performance electronic Ag particles and efficient semiconductor devices.

KEYWORDS

silver particles, small angle X-ray scattering (SAXS), pore size distribution, *in-situ* heating X-ray diffraction (XRD), sintering, silicon solar cells

1 Introduction

With the increasing demand of clean sustainable energy, photovoltaic (PV) has gradually become a competitive alternative for traditional fossil energy. As the technology with the largest proportion in the photovoltaic industry, crystalline silicon (c-Si) solar cells have received great attention worldwide [1]. Semiconductor metallization is a process of forming contact through screen printing and sintering, which is needed to manufacture c-Si solar cell devices [2]. The silver paste was utilized for the fabrication of front electrodes due to its high electrical conductivity, excellent welding capabilities, and remarkable chemical stability [3]. Optimal Ag paste can effectively reduce resistance by electrode densification and contact improvement, which improves device performance [4]. Over the past three decades, the development of c-Si solar cells has been remarkable [5], even if metallization still limits the efficiency improvement of c-Si solar cells. Therefore, the majorization of Ag paste is still an effective way to improve device efficiency.

The effect of Ag paste on c-Si solar cells is critically dependent on designing two high-quality components: the semiconductor-metal contact (the contact interface between the silicon (Si) layer and the Ag layer) and the sintered fingers of Ag particles (conductive network) [3]. Designing these components to minimize electrical losses due to resistance is essential. Ag paste typically consists of spherical Ag particles, glass frits, and organic carrier [6]. As the highest proportion in Ag paste, Ag particles play a crucial role in electrical properties for their significant impact during the sintering process [7]. To establish an optimal connection, the sintering process necessitates the execution of four distinct stages: firstly, the volatilization of the organic phase; secondly, the melting of glass frits and Ag particles; thereafter, the etching of the Si nitride layer by lead in glass frits; and finally, the formation of a metal-semiconductor connection following the cooling down period [3, 8]. Ag particles affect the sintering process dramatically, hence controlling the morphology and structure of Ag particles to obtain different properties is important [9]. In previous studies, it was found that the morphology and particle size of Ag particles affect its sintering performance [9, 10]. Generally, Ag particles with nano-size can be added to improve sintering activity and to densify the sintered bulk. This is due to

Address correspondence to Dong Zhou, zhoudong@mail.iasf.ac.cn; Yuan Lin, linyuan@iccas.ac.cn; Feng Pan, panfeng@pkusz.edu.cn

the nanometer size effects of particles materials. As the size decreases, the specific surface area increases and the melting temperature decreases [11–13]. However, the specific surface area of nanoscale powders is extremely high, which makes the viscosity of the slurry too high to achieve precision printing [14]. Therefore, improving the sintering performance by changing the structure of Ag particles rather than using nanoscale Ag particles is an effective way to improve device performance. However, there is limited research on the internal structure of Ag particles.

In order to regulate the sintering performance of Ag particles at similar size, the internal structure of Ag particles was designed. Ag particles were usually prepared by liquid-phase reduction method [15–19]. There are many methods for preparing hollow powder materials, especially the template method [20–22]. In this work, a type of low crystalline hollow spherical Ag particles (marked as SP-A) was synthesized by adding sodium dodecyl benzene sulfonate (SDBS) and isohexadecanol, while a type of traditional high crystalline solid Ag particles (marked as SP-B) was synthesized. The SP-A have a better sintering activity than SP-B. These two types of Ag particles were used to prepare the front Ag paste for solar cells (marked as Paste-A and Paste-B, respectively), which were printed on polycrystalline Si chips to make c-Si solar cells (marked as Cell-A and Cell-B, respectively) [23]. The Cell-A obtained a high short-circuit current density (j_{sc}) and a low R_s, while the Cell-B obtained a lower j_{sc} and a higher R_s. As the result, the filling factor (FF) of Cell-A was 79.12% and the power conversion efficiency (PCE) of it was 19.26%, higher than Cell-B (FF of 76.66 % and PCE of 18.23%). This exhibits a competitive advantage when compared to cells of the same type in other related works. Then the difference of structure and sintering activity of SP-A and SP-B and the sintered Ag fingers of Cell-A and Cell-B were explored by multiple detection methods.

2 Experimental

2.1 Materials and devices preparation

Preparation of Ag particles: The Ag particles were prepared by liquid-phase reduction method. The fabrication process of Ag particles requires three steps. Firstly, Ag nitrate was dissolved in deionized water (concentration was 0.1 M). Then, ammonia monohydrate was added with twice the molar ratio of Ag nitrate. Finally, additives were added into the solution to obtain oxidant solution. The reductant solution was prepared by dissolving ascorbic acid in water (concentration was 0.07 M). Equipped with a hedging and confluence device, the reducing solution and oxidizing solution were mixed to obtain a suspension containing Ag particles. After separating the solid and liquid, the precipitate was cleaned to obtain Ag particles. To make the surface of Ag particles hydrophobic, an emulsion composed of stearic acid, benzotriazole, sodium dodecyl sulfate, alcohol ethoxylate 3, and sodium hydroxide was used to coat these particles. Finally, the Ag particles were dried and mechanically stirred, and ethanol solution of stearic acid and its derivatives were added during stirring for secondary coating, and then were cleaned and dried to obtain a sample of Ag particles. As surfactant and cosurfactant, SDBS and isohexadecanol were added into the oxidized liquid to fabricate SP-A. Moreover, Na_2SO_3 was added into the oxidized liquid to prepare the control group of SP-B.

Preparation of Ag paste: Ag paste was prepared by mixing 90% Ag particles, 8% organic carrier (containing resin and solvent), and 2% glass frits (containing Pb, Si, Te, W, etc.) and using a homogenizer and a three rolls machine to disperse it thoroughly. Paste-A and Paste-B were used SP-A and SP-B, respectively.

Manufacturing of polycrystalline Si solar cells: The cells were manufactured by using Paste-A and Paste-B with similar procedures and were marked as Cell-A and Cell-B, respectively. The manufacturing process of c-Si solar cells is as follows: By screen printing and co-firing in a belt furnace, Al-Si (made by aluminum paste) and Ag–Si contacts (made by Paste-A and Paste-B, respectively) were formed on the polycrystalline Si wafer (156.75 mm × 156.75 mm). The Si wafers and aluminum paste used in this work were commercial products. The electrical parameters of the cells were measured using a pulsed solar simulator (PSL SCD, BERGER Lichttechnik GmbH & Co.KG). A digital source meter (Keithley 2602A) was used for measuring resistance (the resistance was measured after sintering a 0.5 mm × 40 mm × 5 μm silver gate wire printed on an alumina ceramic substrate).

2.2 Materials characterizations

The morphology and structure of the materials and devices were examined by scanning electron microscope (SEM, ZEISS SUPRA-55). The crystalline structures of the samples were analyzed by X-ray diffraction (XRD) measurements with a Bruker D8 Discover diffractometer (Cu Kα radiation with λ = 1.5405(6) Å within the 2θ range of 10°–80°). The Brunauer–Emmett–Teller (BET) analyzer (ASAP 2020M + C) was used to measure the specific surface area of Ag particles on the outer surface. The *in-situ* heating device (Anton Paar, HTK 1200N) for *in-situ* XRD was used to study the structural changes during heating process. Thermal analyses were conducted on a thermogravimetric/differential scanning calorimetry (TG/DSC) analyzer (NETZSCH, STA449F3) and a thermo mechanical analyzer (TMA, METTLER TOLEDO, TMA-SDTA2) to determine the sintering properties and sintering behavior of Ag particles. A three-dimensional (3D) laser confocal scanning microscope (KEYENCE, VK-X200) was used to observe the shape of Ag finger. A focused ion beam (FIB, FEI Scios) equipment was used to analyze the sintering process of Ag particles at different temperatures and the cross section of Ag finger, and an energy-dispersive X-ray spectroscopy (EDX) (Oxford X-Max 170) was used to analysis Ag–Si interface composition. Ultra-small-angle X-ray scattering (USAXS) and small-angle X-ray scattering (SAXS) were used to characterize the internal structure of Ag particles. USAXS was performed at BL10U1 beamline of Shanghai Synchrotron Radiation Facility (SSRF) with 10 keV X-ray energy and Dectris Eiger 4M detector. SAXS was performed at the Institute of Advanced Science Facilities, Shenzhen (IASF) with liquid metal jet source (Ga Kα: 9.24 keV, wavelength: 1.35 Å) and Dectris Pilatus 1 M detector. USAXS data and SAXS data of the same sample were merged for a wider range of scattering vectors. A Malvern-Zetasizer-Nano-ZS90 was used for measuring micelle particle size.

3 Result

Ag particles were synthesized through liquid phase reduction method. After washing and drying, the final sample of Ag particles was obtained by surface smoothing treatment. The surface smoothing treatment was to disperse the agglomerated Ag particles after drying and make their surface smooth of the production of Ag paste. Figure 1(a) illustrates the fabrication process of Ag particles. The overall morphology, surface microstructure, and cross-sectional structure morphology of SP-A are shown in Figs. 1(b)–1(d). The SP-A are spherical particles with a particle size of 1–2 μm, with good dispersibility and no particle agglomeration. The surface of SP-A is relatively rough with many microstructures. The cross-section of SP-A was prepared using FIB, and many pores ranging from tens to hundreds of

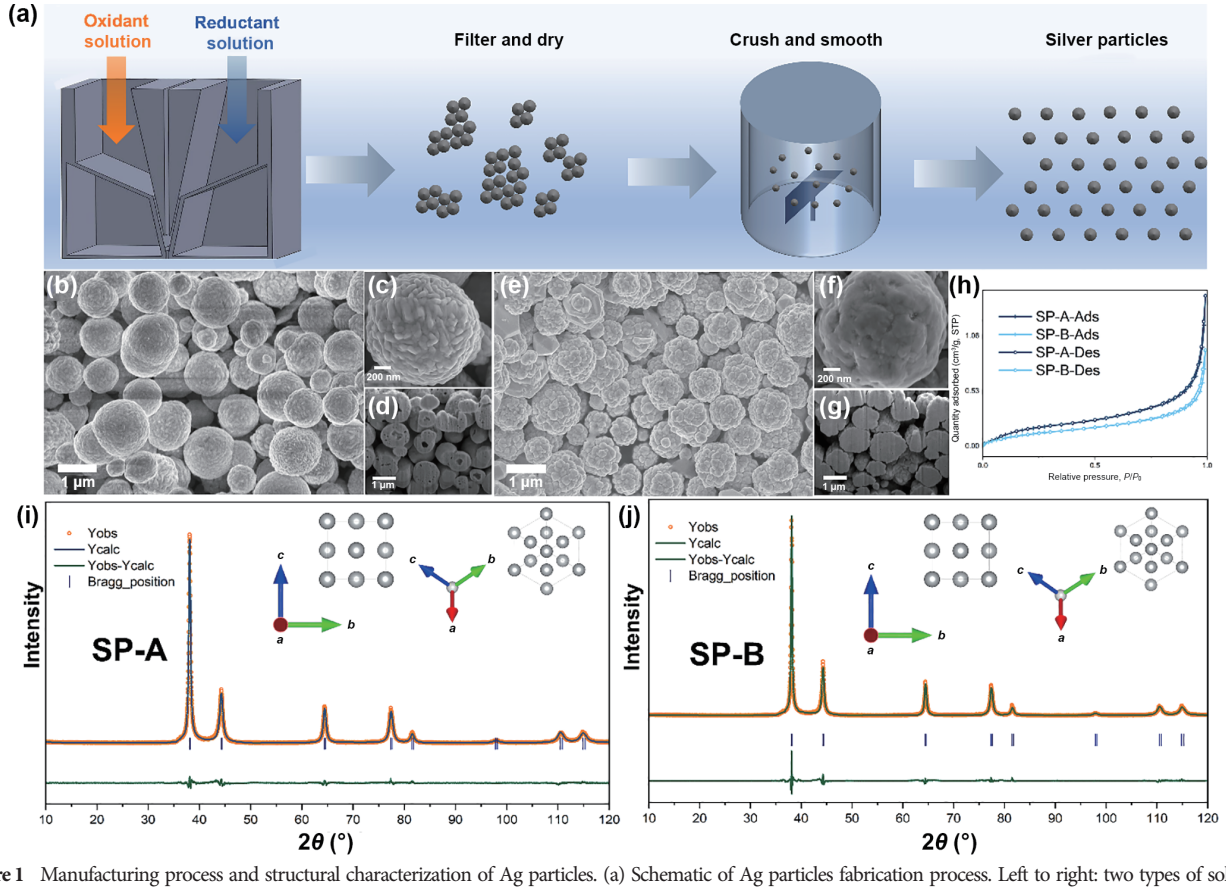

Figure 1 Manufacturing process and structural characterization of Ag particles. (a) Schematic of Ag particles fabrication process. Left to right: two types of solution were mixed through a confluence device, filtered, and dried after surface coating, crushing, and surface smoothing treatment. (b)–(d) The SEM images of the morphology and cross-sectional structure of SP-A. (e)–(g) The SEM images of the morphology and cross-sectional structure of SP-B. (h) The adsorption and desorption isotherms curves of SP-A and SP-B. (i) and (j) The crystal structure characterization of SP-A and SP-B, respectively.

nanometers can be observed. The soft template method obtains special structures by using surfactants with hydrophobic and hydrophilic groups to form micelles or droplets in solution to provide templates for synthesized materials. This type of method has been applied to synthesize various nanomaterials [20–22]. Some surfactants can affect the aggregation and growth of silver particles and provide soft templates [24]. The micelles formed by adding a single SDBS to the solution are relatively small. By adding surfactant (SDBS) and cosurfactant (isohexadecanol) simultaneously, some droplets with large sizes are formed (the size distribution of the droplets is shown in Fig. S1 in the Electronic Supplementary Material (ESM)). Due to the addition of cosurfactants, the structure of the droplets is more stable [25–28]. In addition, the convergent mixing method of reductant solution and oxidant solution makes an intense reaction (Fig. 1(a)), which is conducive to generating smaller silver microcrystals. The presence of pores inside SP-A may attributed to these stable droplets and the smaller silver microcrystals. Figures 1(e)–1(g) show the overall morphology, surface microstructure, and cross-sectional structure morphology of SP-B. SP-B are also spherical particles with a particle size of 1–2 μm, with good dispersibility and no particle agglomeration. Compared to SP-A, the surface structure size of SP-B is relatively large. The cross-sectional SEM image of SP-B shows that SP-B are solid particles with a small number of nanopores but without macroscopic pores. Figure 1(h) shows the adsorption and desorption isotherms curves of SP-A and SP-B, with a specific surface area of 0.7282 m^2/g for SP-A and 0.4877 m^2/g for SP-B (the original graph is shown in Fig. S2 in the ESM). To determine the crystal structures of SP-A and SP-B, XRD measurements followed by Rietveld refinement on diffraction patterns were performed [29, 30]. As illustrated in Figs. 1(i) and 1(j), both SP-A and SP-B are related to the Ag standard (4-0783) [15]. The structural model with *Fm-3m* space group can describe the structure of SP-A and SP-B, in which the Ag is arranged in a face-centered cubic [31]. The characteristic peaks appear with 2θ values at 38.1°, 44.3°, and 64.4°, corresponding to (111), (200), and (220) crystal planes, respectively [15]. According to the refinement results in Table S1 in the ESM, the SP-A possess the initial unit cell parameters of $a = b = c = 4.087$ Å and $V = 68.313$ Å^3, while the SP-B possesses the initial unit cell parameters of $a = b = c = 4.090$ Å and $V = 68.440$ Å^3. The difference in the initial unit cell parameters between SP-A and SP-B is not significant. The sintering activity of particles is closely related to their grain size and specific surface area, due to small grain size with large specific surface area enhances sintering activity [12, 17]. In order to further analyze the difference between SP-A and SP-B, their average grain sizes were calculated. Usually, the microcrystalline size of particles, at a scale of several tens of nanometers, can be calculated using the Scherrer formula [32]. Scherrer formula can be written as

$$D_c = K\gamma/(B\cos\theta) \quad (1)$$

where K is the Scherrer constant; D_c is the average thickness of the grain perpendicular to the crystal plane direction; B is the width at half peak height of the measured sample diffraction; θ is the Bragg angle; and γ is the X-ray wavelength, which is 1.54056 Å. For spherical particles, the value of K is 0.89. By Eq. (1), the average grain sizes of SP-A and SP-B can be calculated to be 23.86 and 30.56 nm, respectively (Table S2 in the ESM). Qualitatively, this result is consistent with the SEM image. Due to the average grain size of SP-A being smaller than that of SP-B, the surface of SP-A would be rougher than that of SP-B. It is consistent with the BET results (Fig. 1(h)). Research found that the larger the specific surface area of the powder, the more favorable it is for sintering

[11, 12, 17]. In brief, the above results indicated that the sintering activity of SP-A should be higher than that of SP-B.

In order to further characterize the differences in the internal structure of SP-A and SP-B, USAXS and SAXS were used and their results were merged for the same samples. Figure 2(a) depicts FIT2D data processing of USAXS for SP-A and SP-B, respectively. Subsequent data calculations are based on the results of the Guinier–Porod model calibration [33, 34]. Figure 2(b) demonstrates the relationship between I and q of SP-A and SP-B. According to the theories of Guinier and Porod [35, 36], the measurable range of pore diameter can be written as

$$q = 4\sin\theta/\lambda \quad (2)$$

$$D = 2/q \quad (3)$$

where q is the scattering vector; D is the pore diameter; λ is the X-ray wavelength; θ is the scattering angle.

The measuring range of q in this work ranges from 0.014958 to 2.3358 nm^{-1}, corresponding to the range of D from 2.690 to 420.055 nm according to Eq. (3). The slope of I in the log-log plot decreases with the increase of q, which indicates that there is an electron density contrast between the pores and the Ag body in the Ag particles. Figure 2(c) shows the curves of $\ln(I)$–q^2 and $\ln(Iq^4)$–q^2 for SP-A and SP-B. By calculating the slope of the high q part of the $\ln(Iq^4)$–q^2 curves, the invariant K can be obtained [37], as well as the invariant Q by integrating Iq^2 [38]. Based on the above results, the pore size distribution (PSD) of Ag particles is calculated using the log-normal distribution method (related calculation results are shown in Table S3 in the ESM) [39]. Figure 2(d) displays the results of PSD (the full pore diameter distribution is added in Fig. S3 in the ESM). It is obvious that the PSD distribution of SP-A is wider than that of SP-B, and the overall pore size of SP-A is much larger than that of SP-B. The PSD results are consistent with the cross-sectional morphology of the Ag particles in Figs. 1(d) and 1(g). Using software (nano measurer) to measure the scale of pores for SP-A, 169 visible pores were measured, and the counting frequency of their pore size range is consistent with the PSD results of SAXS (Fig. S4 in the ESM). On the one hand, the pores with diameters of tens to hundreds of nanometers in SP-A may affect the Ostwald ripening, which makes the grain size of Ag particles smaller. On the other hand, it may provide additional power to promote sintering [40, 41].

To investigate the behavior of two types of Ag particles sintering processes, *in-situ* heating XRD measurement and thermal analysis were applied. Figures 3(a) and 3(b) illustrate the *in-situ* heating XRD results of SP-A and SP-B. It is obvious that the peak intensity of SP-A increases suddenly between 170–180 °C, while the peak intensity of SP-B increases suddenly between 220–240 °C. This indicates that the grain coarsening temperature of SP-A is lower than that of SP-B. The value of Dc at each temperature is calculated by Eq. (1), and the result is reflected in Fig. 3(c). The curve of SP-A shows a mutation between 170 and 180 °C. The curve of SP-B has a steep curve at 220–240 °C, followed by a gentle rise as SP-A. It means that the temperature of grain coarsening in SP-A is lower than that in SP-B, and the sintering activity of SP-A is better. After the *in-situ* heating XRD test, SP-A sintered into a dense network, while the SP-B is still in the stage of sintering neck expansion and has not connected into a sheet-like network (shown in Fig. S5 in the ESM). This may be due to the pores inside the SP-A particles, which cause them to expand outward and sinter with surrounding particles during the heating process. The DSC curves of SP-A and SP-B can be seen in

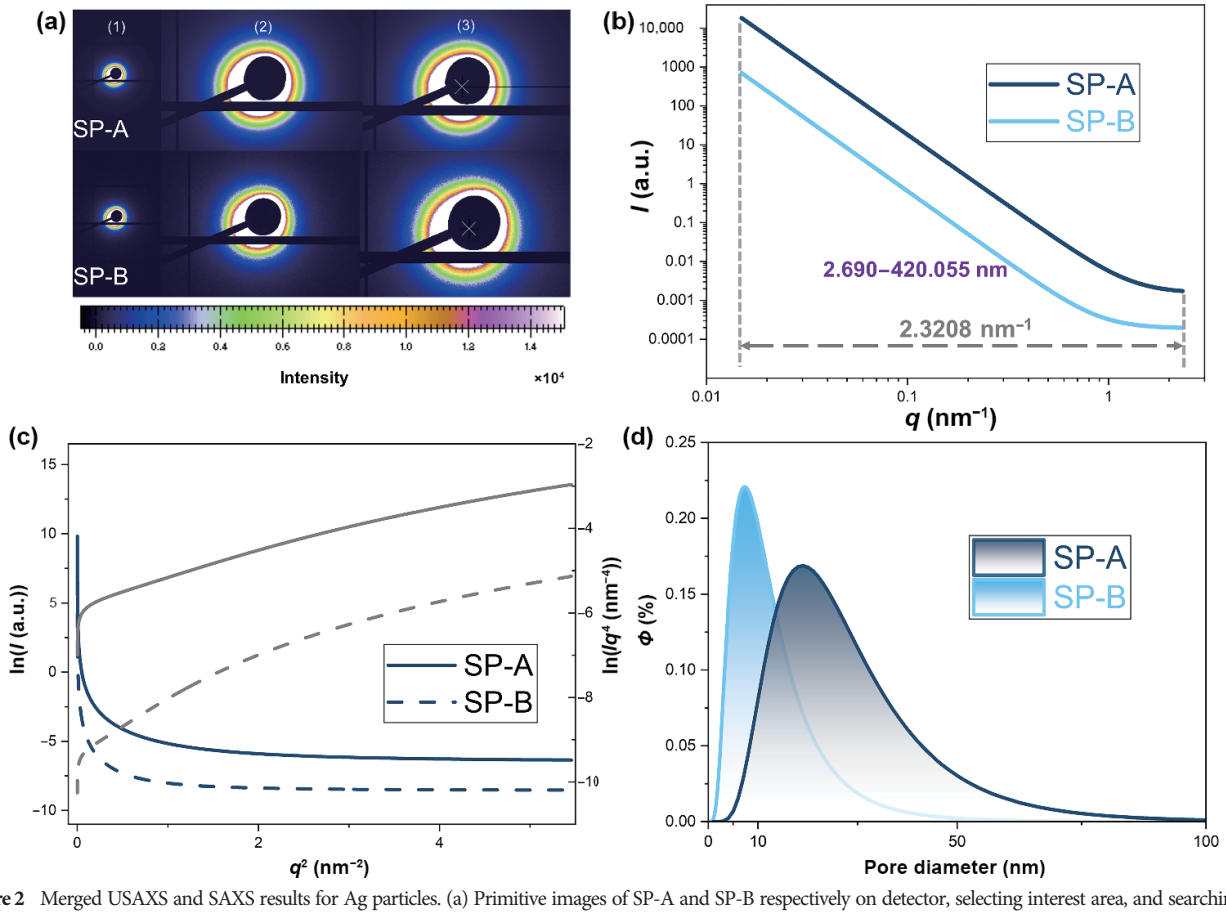

Figure 2 Merged USAXS and SAXS results for Ag particles. (a) Primitive images of SP-A and SP-B respectively on detector, selecting interest area, and searching for center coordinate points. (b) The relationship between I and q after calibration with the Guinier–Porod model. (c) The curves of $\ln(I)$–q^2 and $\ln(Iq^4)$–q^2 for SP-A and SP-B, respectively. (d) The PSD was calculated using the log-normal distribution method in the pore diameter range from 0 to 100 nm.

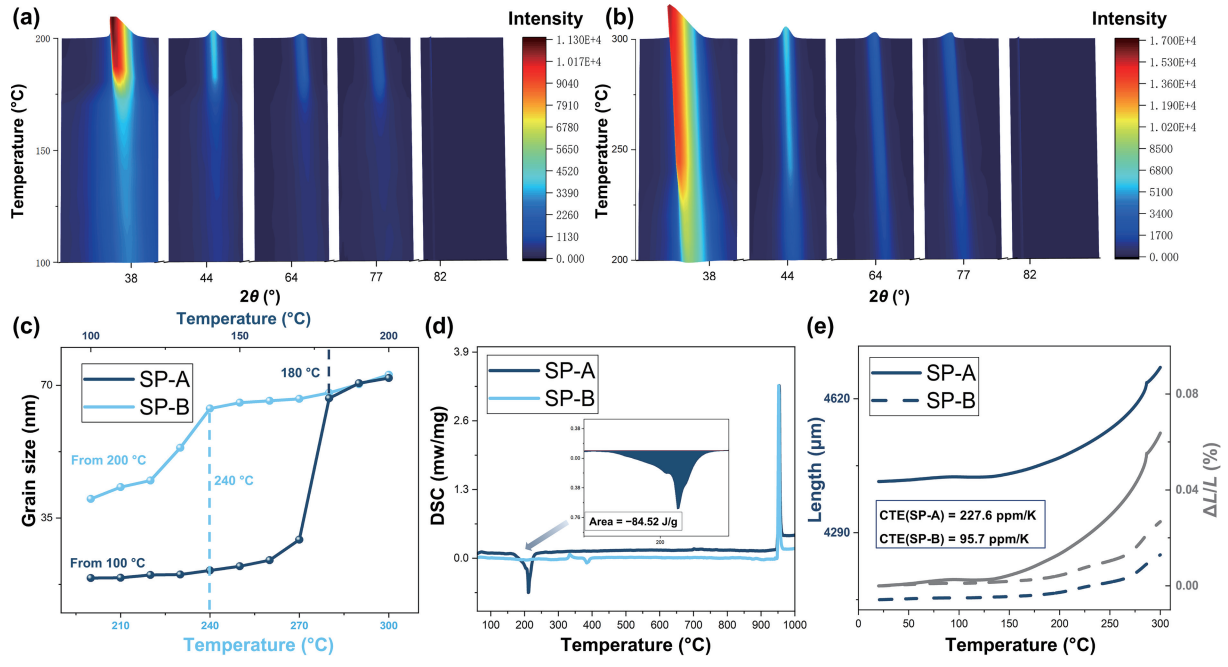

Figure 3 *In-situ* heating XRD measurement and thermal analysis characterizations of Ag particles. (a) and (b) *In-situ* heating XRD spectra of SP-A and SP-B, respectively. (c) The graph of Ag particles grain size variation with temperature. (d) The DSC curves of Ag particles. (e) The TMA and volume change rate curves of Ag particles.

Fig. 3(d) and reveal that SP-A have a significant exothermic peak from 170 to 200 °C, while SP-B is relatively flat with no obvious peaks. This exothermic peak may be beneficial for the sintering of silver particles and may change their grain size [42–46]. To further understand the sintering process, TMA was used to study the volume change of Ag powder during the sintering process. As shown in Fig. 3(e), the volume expansion of SP-A with temperature change is faster than that of SP-B. The coefficient of thermal expansion (CTE) for SP-A from 20 to 300 °C is 227.6 ppm/K, which is 2.37 times that of SP-B (95.7 ppm/K). A high CTE could provide an additional pressure during the sintering process, facilitating sintering between particles [47, 48]. Due to the internal pores, the SP-A particles undergo thermal expansion and sintering with other particles, consistent with the SEM results after *in-situ* sintering. These results indicate that the pores inside SP-A are beneficial for sintering.

To intuitively investigate the sintering process of these two types of Ag particles, FIB was used to prepare the cross-section of the Ag sintered body, and electron beam and ion beam imaging were used for observation. Figures 4(a)(1)–4(a)(6) show the cross-section morphology of electron beam imaging of SP-A sintered body after heating at different temperatures for 3 min. After heating at 250 °C, large sintering necks have been formed between the Ag particles, which are interconnected to form a network, and the small pores inside the Ag particles have merged into large pores. From 300 to 400 °C, the number of independent small pores in the sintered body decreases while the size of the pores increases, which is a process of pore merging. When the heating temperature exceeds 500 °C, the pores of the sintered body continue to disappear, and this stage is a densification process [45, 46, 48]. The results of the same process for SP-B are shown in Fig. 4(b). After 250 °C heating, only a few particles form sintering necks between them, while most are independent. As the temperature rises to 300 °C, sintering necks form between almost all particles and some tiny pores appear inside these particles. From 400 to 500 °C, the sintered body of SP-B is still in the stage of the sintering neck expanding, and the gaps between particles have not significantly decreased [46, 48]. Meanwhile, we can see that at this stage, the small pores inside the particles merge into spherical larger pores. At temperatures above 600 °C, the sintered body begins to densify with the disappearance of pores. After heating at 700 °C, the pores of the SP-B sintered body become smaller and fewer, but still more than those of the SP-A sintered body. Comparing the heating results of SP-A and SP-B at different temperatures, the temperature at which sintering begins of SP-A is lower than that of SP-B, and the sintered body of SP-A is denser than that of SP-B after heating at the same temperature. From the process of pores merging to the disappearance, the results are consistent with the distribution results of USAXS and SAXS. There are several nanometers of pores in SP-B, but due to their small size, they have almost no effect on sintering. The large pores in SP-A play a significant promoting role during sintering.

The SEM images (Figs. 4(a) and 4(b)) are used to observe the changes in the internal pores of the sintered body during the sintering process. Electronic imaging is limited and cannot observe the changes in grain size during sintering. Since the interaction between ions and atoms depends on the grain orientation of the crystal, ion beam imaging and electron beam imaging can complement each other to obtain more comprehensive material characteristics [49]. To analyze the changes in grain size and orientation of Ag particles and sintered bodies during the sintering process, ion beams were used to observe the same cross-section of the samples in Figs. 4(a) and 4(b). The ion beam imaging results of the cross-section for SP-A after heating at different temperatures are represented in Fig. 4(c). Observing the particle cross-section of SP-A heated at 250 °C, grains of SP-A have obvious orientation. Compared to unheated SP-A particles with fine and irregularly distributed grains (shown in Fig. S6 in the ESM), their grain size increases and the grains are arranged radially around the internal pores of the particles. This is similar to the sintering behavior of Ag nanoparticles [50]. As the heating temperature increases to 700 °C, the grains of SP-A particles further coarsen. During the heating process, the radial grains at the formation position of the sintering neck are still retained. Figure 4(d) shows the ion beam imaging results of the cross-section for SP-B after heating at different temperatures. After heating at 250 and 300 °C, the internal grains of SP-B particles are similar to those of unheated ones, and they are fine and irregularly

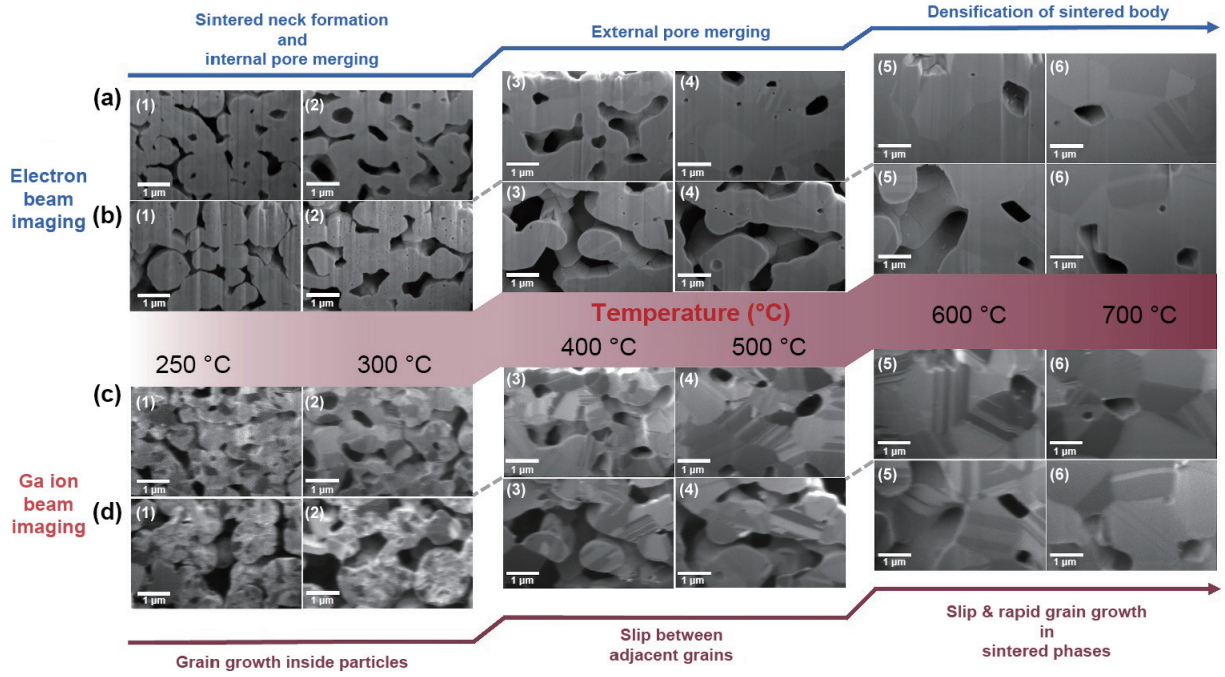

Figure 4 The cross-section images by electron and ion beam imaging of Ag particles after different temperatures heating. (a) and (b) The cross-section SEM images of SP-A and SP-B, respectively. (c) and (d) The cross-section ion imaging images of SP-A and SP-B, respectively.

distributed grains. When the heating temperature increases to 350 °C, stripe grains appear in the sintered body (shown in Fig. S7 in the ESM), which is consistent with the DSC results of SP-B. Unlike the radial grains of SP-A, the strip like grains of SP-B traverse the entire SP-B particle (the surface images of grain orientation of the sintered body for SP-A and SP-B are displayed in Fig. S8 in the ESM). As the heating temperature increases, the grain size of the sintered body for SP-B continues to increase same as the heating process of SP-A.

In conclusion, SP-A can start sintering at lower temperatures and its sintering activity is better than SP-B. Sintered at the same temperature, SP-A can form a denser sintered body (reflected in Fig. S9 in the ESM). The excellent sintering performance of SP-A is attributed to the pores structure and the small grains around these pores, which provide more defects and accelerate the Ag diffusion rate. This structure forms many radial grain structures between particles during the sintering process, providing faster channels for atomic movement [43–45, 48]. This excellent sintering performance of SP-A enables rapid sintering at lower temperatures to form a good connection with the substrate (for c-Si solar cell, the substrate is Si wafer), as well as the sintered body itself [51]. The metallization of c-Si solar cells is completed by rapid sintering in an infrared sintering furnace, and the high sintering activity of SP-A may cause the contact between Ag and Si closer as well as the contact between Ag particles, thereby forming a better contact [52].

The SP-A and the SP-B were mixed respectively with the same glass frits powder and organic phase to produce Ag paste (marked as AP-A and AP-B), and the AP-A and the AP-B were printed on polycrystalline Si wafers, then an infrared sintering furnace was used to produce polycrystalline c-Si solar cells, labeled as Cell-A and Cell-B, respectively. The Real photo and 3D laser images of polycrystalline Si solar cell in this work are shown in Fig. S10 in the ESM, and the photovoltaic performance parameters of Cell-A, Cell-B, and same type devices in other works are listed in Table 1 [53, 54]. The cell made by commercial silver paste was labeled Cell-commercial. In order to make the data statistically meaningful, a statistical analysis of the efficiency for Cell-A, Cell-B, and Cell-commercial was produced and drew a box plot to display the result. The statistical data on the efficiency of cells are shown in Fig. S11 in the ESM. Overall, both the highest and average PCE of Cell-A are higher than that of Cell-B. Compared with cells made by commercial silver paste, the PCE of Cell-A is competitive (the raw data is shown in Tables S4– S6 in the ESM).

Figure 5(a) compares photovoltaic characteristic parameters between Cell-A and Cell-B. There is not much difference in open circuit voltage (V_{oc}) between these two cells due to the same glass frits, while the R_s of Cell-A is smaller than that of Cell-B [55, 56]. This results in high j_{sc}, FF, and PCE for Cell-A. The difference of R_s may be due to the difference of contact between Ag finger and Si, as well as Ag finger sintered body. Figures 5(b) and 5(e) display the 3D laser topography of the Ag fingers of Cell-A and Cell-B. FIB was used to prepare the cross-sectional samples of Ag fingers for Cell-A and Cell-B to observe their state after sintering. As shown in Figs. 5(c) and 5(f), the Ag fingers of Cell-A are denser than those of Cell-B. Meanwhile, many radial grains in the Ag finger of Cell-A, while the Ag finger of Cell-B has no this structure, consistent with the structure in Fig. 4. The silver pastes produced by SP-A and SP-B are labeled as paste-A and paste-B, respectively. The resistance of the printed wide finger lines made by paste-A, paste-B, and commercial silver paste (paste-Commercial) was measured through a four-wire method to obtain their conductivity (shown in Fig. S12 in the ESM) [57]. The conductivity of paste-A after sintering is 1.536×10^7 S/m, which is higher than that of paste-B (1.331×10^7 S/m). This is consistent with the previous results. The conductivity of paste-A after sintering is slightly lower than that of paste-Commercial (1.78×10^7 S/m). The Ag–Si contact part of Cell-A and Cell-B is reflected in Figs. 5(d) and 5(g). The Ag–Si contact of Cell-A is tight, while the Ag–Si contact of Cell-B has some voids. In addition, there are differences in the silver and silicon layer interfaces between Cell-A and Cell-B. There are many Ag nanoparticles in the interface glass layer of Cell-A. On the contrary, there is little Ag nanoparticle in the interface glass layer of Cell-B. The SP-A are sintered at lower temperatures, and this high sintering activity may allow SP-A for better melting into the glass during the fast-firing process, which is conducive to the precipitation of Ag nanoparticles in the interface glass layer. Energy dispersive spectrometer (EDS) point-scan

Table 1 PV performance parameters of Cell-A, Cell-B, and other same type cells

Cell	V_{oc} (V)	j_{sc} (mA/cm^2)	R_s (Ω)	FF (%)	PCE (%)
Cell-A	0.6432	37.84	0.002726	79.118	19.26
Cell-B	0.6435	36.89	0.004561	76.769	18.23
Cell-commercial-Ag	0.6382	37.73	0.002483	79.071	18.98
Other Cell-1[53]	0.6266	36.78	—	78.9	18.1
Other Cell-2 [54]	0.6270	35.59	—	78.99	18.07

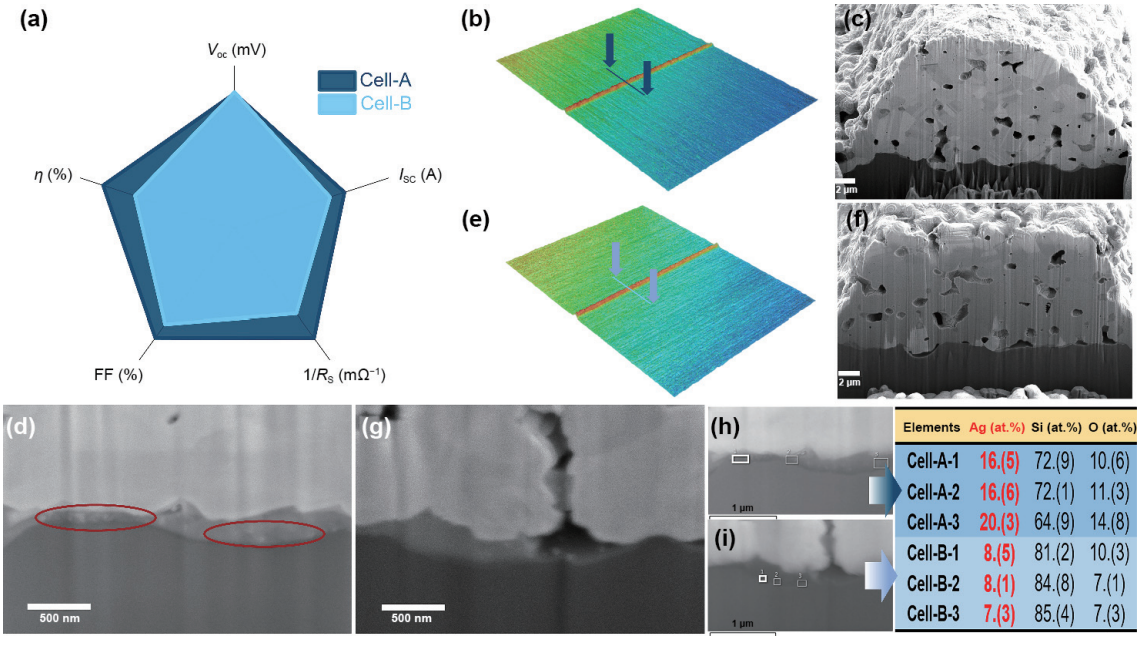

Figure 5 Performance comparison of Cell-A and Cell-B and the cross-section structure of Ag fingers for them. (a) The comparison of photovoltaic parameters for Cell-A and Cell-B. (b)–(d) The 3D laser image and the cross-sectional morphology of Ag finger for Cell-A. (e)–(g) The 3D laser image and the cross-sectional morphology of Ag finger for Cell-B. (h) and (i) the EDS point-scan results of Cell-A and Cell-B.

mode is used to determine the content of elements in the glass layer. It is obvious that the percentage of Ag in the interface glass layer of Cell-A is higher than that of Cell-B (the original report is shown in Fig. S13 in the ESM). The Ag nanoparticles in the glass layer can improve the silver silicon contact and reduce the R_s [58–60]. It proves that SP-A with high sintering activity can promote the formation of good contact at the Ag Si interface. These result in a low R_s of 2.72 mΩ for Cell-A, while a higher R_s of 4.56 mΩ for Cell-B. In addition, the j_{sc} of Cell-A (37.84 mA/cm^2) is also higher than that of Cell-B (36.89 mA/cm^2). As a result, the FF of Cell-A is 79.12%, and the PCE of it is 19.26%, higher than Cell-B (FF of 76.66 % and PCE of 18.23%). Compared to SP-B, the SP-A with high sintering activity caused by internal pores is more conducive to forming high-quality Ag fingers and Ag–Si interface, thereby improving the PCE of c-Si solar cells. Although the R_s of Cell-A is slightly higher than the R_s of the cell made of commercial materials, the V_{oc} (0.6432 V) and j_{sc} (37.84 mA/cm^2) of Cell-A are both higher than those of the cell made of commercial materials (0.638 V and 37.73 mA/cm^2, respectively). It makes the maximum power (Pmpp) of Cell-A (4.723 W, shown in Table S4 in the ESM) higher than Pmpp of the cell made of commercial materials (4.654 W, shown in Table S6 in the ESM). The result is that the PCE of Cell-A is higher than that of the cell made of commercial materials. Compared to the cell made by commercial materials, the absolute efficiency improvement (AEI) of SP-A is 0.28% and relative efficiency improvement (REI) is 1.4%, which is significant compared to other similar work (shown in Fig. S14 in the ESM) [61–63]. Moreover, the PCE of the Cell-A is competitive compared to the same type of polycrystalline silicon cells in other works (shown in Fig. S15 in the ESM).

4 Conclusions

In summary, using a simple method, we successfully synthesized highly dispersed low crystalline SP-A with internal pores structure. The structure and the distribution of internal pores for SP-A were studied by XRD, SAXS, and USAXS. Compared to traditional Ag particles with no obvious internal pores, pores range from tens of nanometers to hundreds of nanometers inside SP-A. Due to the internal pores, the weakening of Ostwald ripening leads to the small D_c of SP-A, and the CTE is high during heating. By observing the morphology and grain changes of SP-A at different heating temperatures, it was found that small grains around the internal pores gradually merge and coarsen during heating, then formed radial large grains and grain boundaries. This provides a faster path for the diffusion of Ag. Therefore, SP-A has excellent sintering performance, which can form a tighter sintered body and achieve better contact effect. Finally, a polycrystalline c-Si solar cell was made using SP-A, with low R_s of 2.72 mΩ and a high PCE of 19.26%. In particular, this work provides a method for characterizing the internal structure of Ag particles and analyzing the influence of internal pores structure on sintering, which is of great significance for the development of high-performance electronic Ag particles and efficient semiconductor devices.

Acknowledgements

The author would thank the support of the Soft Science Research Project of Guangdong Province (No. 2017B030301013), the Guangdong Innovative Team Program (No. 2013N080), and the Guangdong Province Major Talent Introducing Program (No.

2021QN020687). USAXS experiments supported by Dr. Feng Tian and BL10U1 beamline at SSRF are also acknowledged.

Electronic Supplementary Material: Supplementary material (particle size distribution of droplets formed by surfactants and cosurfactants; adsorption and desorption isotherms curves of SP-A and SP-B; the PSD calculated by SAXS and the PSD of SP-A measured and fitted through SEM image; SEM images of the sintered body after *in-situ* XRD heating test; the cross-section images by ion beam imaging and SEM images of Ag particles and original ion beam images of Figs. 4(c1) and 4(d1); the cross-section images by ion beam imaging of Ag particles; the cross-section images by electron and ion imaging of SP-B; the grain orientation of the sintered body for SP-A and SP-B after 400 °C heating; the surface morphology of sintered bodies for SP-A and SP-B after heating at different temperatures; real photo and 3D laser images of polycrystalline silicon solar cells in this work; the statistical data on the efficiency of Cell-A, Cell-B, and Cell-commercial; the R_s of Cell-A, Cell-B, and Cell-commercial and the conductivity of paste-A, paste-B, and commercial silver paste after sintering; the original report of the EDS point-scan results of Cell-A and Cell-B; refined cell parameters of SP-A and SP-B and standard PDF card parameters; XRD results and D_c of SP-A and SP-B; SAXS related calculation results; the raw data of photovoltaic performance of the cells made by SP-A, SP-B, and commercial paste) is available in the online version of this article at https://doi.org/10.1007/s12274-023-6163-3.

References

[1] Helveston, J. P.; He, G.; Davidson, M. R. Quantifying the cost savings of global solar photovoltaic supply chains. *Nature* **2022**, *612*, 83–87.

[2] Buiting, A. G. M.; Thompson, J.; van der Keur, D.; Schmal-Bauer, W. C.; Bertina, R. M. Procoagulant activity of endocardial vegetations and blood monocytes in rabbits with streptococcus sanguis endocarditis. *Thromb. Haemost.* **1989**, *62*, 1029–1033.

[3] Schubert, G.; Fischer, B.; Fath, P. Formation and nature of Ag thick film front contacts on crystalline silicon solar cells. *Proc. 18th Eur. Photovoltaic Sol. Energy Conf.*, 2002, pp 343–346.

[4] Yang, Y.; Seyedmohammadi, S.; Kumar, U.; Gnizak, D.; Graddy, E. D.; Shaikh, A. Screen printable silver paste for silicon solar cells with high sheet resistance emitters. *Energy Procedia* **2011**, *8*, 607–613.

[5] Deng, W. W.; Ye, F.; Xiong, Z.; Chen, D. M.; Guo, W. W.; Chen, Y. F.; Yang, Y.; Altermatt, P. P.; Feng, Z. Q.; Verlinden, P. J. Development of high-efficiency industrial p-type multi-crystalline PERC solar cells with efficiency greater than 21%. *Energy Procedia* **2016**, *92*, 721–729.

[6] Hang, K. W.; Wang, Y. L. Glass composition and its use in conductive silver paste. U. S. Patent 2, 013, 021, 114, November 14, 2013.

[7] Fu, M.; Li, H. Y.; Wang, Y.; Fan, L.; Chen, D.; Feng, Z. Study on the synthesis and performances of ultrafine silver powder used as silicon solar cell front silver contacts. *Mater. Sci. Forum* **2016**, *852*, 378–384.

[8] Fields, J. D.; Ahmad, M. I.; Pool, V. L.; Yu, J. F.; Van Campen, D. G.; Parilla, P. A.; Toney, M. F.; van Hest, M. F. A. M. The formation mechanism for printed silver-contacts for silicon solar cells. *Nat. Commun.* **2016**, *7*, 11143.

[9] Muchmore, P. Collections may depend on your own attitudes. *Dent. Econ.* **1982**, *72*, 51–54.

[10] Li, W.; Yu, C. X.; Wang, Y. K.; Yao, Y.; Yu, X. L.; Zuo, C.; Yu, Y. Experimental investigation of effect of flake silver powder content on sintering structure and properties of front silver paste of silicon solar cell. *Materials* **2022**, *15*, 7142.

[11] Zhang, X. F.; Liu, Z. G.; Shen, W.; Gurunathan, S. Silver nanoparticles: Synthesis, characterization, properties, applications, and therapeutic approaches. *Int. J. Mol. Sci.* **2016**, *17*, 1534.

[12] Shen, W. F.; Zhang, X. P.; Huang, Q. J.; Xu, Q. S.; Song, W. J. Preparation of solid silver nanoparticles for inkjet printed flexible electronics with high conductivity. *Nanoscale* **2014**, *6*, 1622–1628.

[13] Sundaram, D.; Yang, V.; Yetter, R. A. Metal-based nanoenergetic materials: Synthesis, properties, and applications. *Prog. Energy Combust. Sci.* **2017**, *61*, 293–365.

[14] Pasquino, R.; Grizzuti, N.; Maffettone, P. L.; Greco, F. Rheology of dilute and semidilute noncolloidal hard sphere suspensions. *J. Rheol.* **2008**, *52*, 1369–1384.

[15] Avramović, L.; Pavlović, M. M.; Maksimović, V. M.; Vuković, M.; Stevanović, J. S.; Bugarin, M.; Nikolić, N. D. Comparative morphological and crystallographic analysis of electrochemically- and chemically-produced silver powder particles. *Metals* **2017**, *7*, 160.

[16] Gebauer, J. S.; Treuel, L. Influence of individual ionic components on the agglomeration kinetics of silver nanoparticles. *J. Colloid Interface Sci.* **2011**, *354*, 546–554.

[17] Sangsuk, S. Preparation of high surface area silver powder via Tollens process under sonication. *Mater. Lett.* **2010**, *64*, 775–777.

[18] Jose, M.; Sakthivel, M. Synthesis and characterization of silver nanospheres in mixed surfactant solution. *Mater. Lett.* **2014**, *117*, 78–81.

[19] Khanna, P. K.; Singh, N.; Kulkarni, D.; Deshmukh, S.; Charan, S.; Adhyapak, P. V. Water based simple synthesis of re-dispersible silver nano-particles. *Mater. Lett.* **2007**, *61*, 3366–3370.

[20] Wang, Q. H.; Zhu, Y. X.; Xue, J.; Zhao, X. S.; Guo, Z. P.; Wang, C. General synthesis of porous mixed metal oxide hollow spheres with enhanced supercapacitive properties. *ACS Appl. Mater. Interfaces* **2016**, *8*, 17226–17232.

[21] Liu, N.; Zhao, S. P.; Yang, Z. L.; Liu, B. Patchy templated synthesis of macroporous colloidal hollow spheres and their application as catalytic microreactors. *ACS Appl. Mater. Interfaces* **2019**, *11*, 47008–47014.

[22] Wu, P.; Du, N.; Zhang, H.; Zhai, C. X.; Yang, D. R. Self-templating synthesis of SnO_2-carbon hybrid hollow spheres for superior reversible lithium ion storage. *ACS Appl. Mater. Interfaces* **2011**, *3*, 1946–1952.

[23] Zhang, B.; Li, Y. S.; Chen, Y. J.; Chen, H. B.; Zhu, C.; Liu, J.; Lin, Y.; Pan, F. Interface tuning through the MoO_3 additive in Al paste to enhance the performance of crystalline silicon solar cells. *ACS Appl. Energy Mater.* **2022**, *5*, 13254–13260.

[24] Xu, J.; Zhu, X. Z.; Xu, L. H.; Kan, C. X.; Shi, D. N. Template-directed growth of Ag nanostructures: Soft templates *versus* hard templates. *Nanoscale* **2023**, *15*, 1687–1694.

[25] Tuin, G.; Stein, H. N. Adsorption of ionic surfactant on polystyrene particles in the absence and presence of cosurfactant. *Langmuir* **1994**, *10*, 1054–1059.

[26] Sarma, S.; Bora, M.; Dutta, R. K. Effects of alcohol on partition equilibrium of phenol red in micellar solutions and O/W microemulsions of anionic surfactants. *Colloid Surf. A Physicochem. Eng. Asp.* **2005**, *256*, 105–110.

[27] Sarma, S.; Gohain, B.; Dutta, R. K. A visible spectroscopic study of microstructure of O/W microemulsions of anionic surfactants: Effect of cosurfactant. *J. Dispersion Sci. Technol.* **2006**, *27*, 899–905.

[28] Ahsan, T.; Aveyard, R.; Binks, B. P. Winsor transitions and interfacial film compositions in systems containing sodium dodecylbenzene sulphonate and alkanols. *Colloids Surf.* **1991**, *52*, 339–352.

[29] Giannini, C.; Ladisa, M.; Altamura, D.; Siliqi, D.; Sibillano, T.; De Caro, L. X-ray diffraction: A powerful technique for the multiple-length-scale structural analysis of nanomaterials. *Crystals* **2016**, *6*, 87.

[30] Chen, Z. W.; Yang, M. L.; Chen, G. J.; Tang, G. X.; Huang, Z. Y.; Chu, M. H.; Qi, R.; Li, S. M.; Wang, R.; Wang, C. Q. et al. Triggering anionic redox activity in Fe/Mn-based layered oxide for high-performance sodium-ion batteries. *Nano Energy* **2022**, *94*, 106958.

[31] Yan, X. S.; Lin, P.; Qi, X.; Yang, L. Finnis-sinclair potentials for fcc Au-Pd and Ag-Pt alloys. *Int. J. Mater. Res.* **2011**, *102*, 381–388.

[32] Holzwarth, U.; Gibson, N. The Scherrer equation versus the 'debye-scherrer equation'. *Nat. Nanotechnol.* **2011**, *6*, 534.
[33] Hammouda, B. Analysis of the beaucage model. *J. Appl. Crystallogr.* **2010**, *43*, 1474–1478.
[34] Hammouda, B. A new guinier-porod model. *J. Appl. Crystallogr.* **2010**, *43*, 716–719.
[35] Porod, G. Die Röntgenkleinwinkelstreuung von dichtgepackten kolloiden Systemen. *II. Teil. Kolloid-Zeitschrift* **1952**, *125*, 108–122.
[36] Guinier, A.; Fournet, G. *Small-Angle Scattering of X-Rays*; Walker, C. B. , trans. Wiley: New York, 1955.
[37] Li, Z. H.; Gong, Y. J.; Wu, D.; Sun, Y. H.; Wang, J.; Liu, Y.; Dong, B. Z. A negative deviation from Porod's law in SAXS of organo-MSU-X. *Microporous Mesoporous Mater.* **2001**, *46*, 75–80.
[38] Maruyama, I.; Sakamoto, N.; Matsui, K.; Igarashi, G. Microstructural changes in white Portland cement paste under the first drying process evaluated by WAXS, SAXS, and USAXS. *Cem. Concr. Res.* **2017**, *91*, 24–32.
[39] Beaucage, G.; Kammler, H. K.; Pratsinis, S. E. Particle size distributions from small-angle scattering using global scattering functions. *J. Appl. Crystallogr.* **2004**, *37*, 523–535.
[40] Wang, W. S.; Zhen, L.; Xu, C. Y.; Yang, L.; Shao, W. Z. Controlled synthesis of calcium tungstate hollow microspheres via ostwald ripening and their photoluminescence property. *J. Phys. Chem. C* **2008**, *112*, 19390–19398.
[41] Möller, J.; Jacob, K. I.; Schmelzer, J. Ostwald ripening in porous viscoelastic materials. *J. Phys. Chem. Solids* **1998**, *59*, 1097–1103.
[42] Gill, P.; Moghadam, T. T.; Ranjbar, B. Differential scanning calorimetry techniques: Applications in biology and nanoscience. *J. Biomol. Tech.* **2010**, *21*, 167–193.
[43] Rhodes, W. H. Agglomerate and particle size effects on sintering yttria-stabilized zirconia. *J. Am. Ceram. Soc.* **1981**, *64*, 19–22.
[44] Exner, H. E. Role of interfaces in sintering. *Metal Science* **1982**, *16*, 451–456.
[45] Edelson, L. H.; Glaeser, A. M. Role of particle substructure in the sintering of monosized titania. *J. Am. Ceram. Soc.* **1988**, *71*, 225–235.
[46] Coble, R. L. Sintering crystalline solids. I. Intermediate and final state diffusion models. In *Sintering Key Papers*. Sōmiya, S.; Moriyoshi, Y. , Eds.; Springer: Dordrecht, 1990; pp 55–67.
[47] Chen, P.; Raghavan, P.; Yazzie, K.; Fei, H. Y. On the effective coefficient of thermal expansion (CTE) of bilayer/trilayer in semiconductor package substrates. In *2015 IEEE 65th Electronic Components and Technology Conference*, San Diego, USA, 2015, pp 1932–1937.
[48] Kang, S. J. L. Sintering densification, grain growht, and microstructure. *Int. J. Powder Metall.* **2005**, *41*, 73–74.
[49] Li, P.; Chen, S. Y.; Dai, H. F.; Yang, Z. M.; Chen, Z. Q.; Wang, Y. S.; Chen, Y. Q.; Peng, W. Q.; Shan, W. B.; Duan, H. G. Recent advances in focused ion beam nanofabrication for nanostructures and devices: Fundamentals and applications. *Nanoscale* **2021**, *13*, 1529–1565.
[50] Li, M. Y.; Xiao, Y.; Zhang, Z. H.; Yu, J. Bimodal sintered silver nanoparticle paste with ultrahigh thermal conductivity and shear strength for high temperature thermal interface material applications. *ACS Appl. Mater. Interfaces* **2015**, *7*, 9157–9168.
[51] Kim, H. S.; Cho, S. B.; Kim, H.; Kim, D.; Dovrat, M.; Eytan, G.; Huh, J. Y. Electrochemical nature of contact firing reactions for screen-printed silicon solar cells: Origin of "gray finger" phenomenon. *Prog. Photovolt.* **2016**, *24*, 1237–1250.
[52] Schroder, D. K.; Meier, D. L. Solar-cell contact resistance—A review. *IEEE Trans. Electron Devices* **1984**, *31*, 637–647.
[53] Wan, L.; Zhang, C. L.; Ge, K. P.; Yang, X. L.; Li, F.; Yan, W. S.; Xu, Z.; Yang, L.; Xu, Y.; Song, D. Y. et al. Conductive hole-selective passivating contacts for crystalline silicon solar cells. *Adv. Energy Mater.* **2020**, *10*, 1903851.
[54] Zhao, S. X.; Qiao, Q.; Zhang, S.; Ji, J. J.; Shi, Z. R.; Li, G. H. Rear passivation of commercial multi-crystalline PERC solar cell by PECVD Al_2O_3. *Appl. Surf. Sci.* **2014**, *290*, 66–70.
[55] Karpowich, L.; Mayberry, R. W.; Hörteis, M. Impact of glass chemistry on contact formation for silver metallization pastes. In *33rd European Photovoltaic Solar Energy Conference and Exhibition*, Amsterdam, The Netherlands, 2017, pp 617–621.
[56] Eberstein, M.; Falk-Windisch, H.; Peschel, M.; Schilm, J.; Seuthe, T.; Wenzel, M.; Kretzschmar, C.; Partsch, U. Sintering and contact formation of glass containing silver pastes. *Energy Procedia,* **2012**, *27*, 522–530.
[57] Keithley Instruments, Inc. *Making Precision Low Voltage and Low Resistance Measurements* [Online]. https://download.tek.com/document/LV_LR_e-hnbook_91113.pdf (accessed Aug 17, 2023).
[58] Wu, W.; Chan, C.; Lewittes, M.; Zhang, L.; Roelofs, K. Study of carrier transport in silver paste metallized silicon solar cells. *Energy Procedia* **2016**, *92*, 984–989.
[59] Kumar, P.; Aabdin, Z.; Pfeffer, M.; Eibl, O. High-efficiency, single-crystalline, p- and n-type Si solar cells: Microstructure and chemical analysis of the glass layer. *Sol. Energy Mater. Sol. Cells* **2018**, *178*, 52–64.
[60] Li, W.; Wu, T.; Jiao, R. B.; Zhang, B. P.; Li, S. Y.; Zhou, Y.; Li, L. L. Effects of silver nanoparticles on the firing behavior of silver paste on crystalline silicon solar cells. *Colloids Surf. A Physicochem. Eng. Asp.* **2015**, *466*, 132–137.
[61] Deng, D. Y.; Chen, Z. Y.; Hu, Y. L.; Tong, Y. G.; Liang, X. B. Preparation and post-treatment of silver powders for front contact pastes of silicon solar cells. *Int. J. Mater. Res.* **2021**, *112*, 457–464.
[62] Hilali, M. M. The effect of Ag Powder surface topography on the viscoelastic behavior of thick-film Ag gridlines and solar cell performance. In *2018 IEEE 7th World Conference on Photovoltaic Energy Conversion* (*WCPEC*) (*A Joint Conference of 45th IEEE PVSC*, *28th PVSEC & 34th EU PVSEC*), Waikoloa, USA, 2018, pp 2663–2666.
[63] Lan, F.; Bai, J. T.; Wang, H. The preparation of oleylamine modified micro-size sphere silver particles and its application in crystalline silicon solar cells. *RSC Adv.* **2018**, *8*, 16866–16872.